Research Square

Preprints are preliminary reports that have not undergone peer review.
They should not be considered conclusive, used to inform clinical practice,
or referenced by the media as validated information.

Defect Geometry and Concentration Controlled Excitonic Landscape in Monolayer MX 2 - family: A Systematic G 0 W 0 -BSE Study of Chalcogen Vacancies

Shishir Timilsenaa
The University of Texas Rio Grande Valley
Sanju Gupta
Pennsylvania State University
Muhammad Idrees Bhatti
The University of Texas Rio Grande Valley
Nicholas Dimakis
nicholas.dimakis@utrgv.edu

The University of Texas Rio Grande Valley

Article

Keywords:

Posted Date: July 14th, 2026

DOI: https://doi.org/10.21203/rs.3.rs-10120763/v1

License: This work is licensed under a Creative Commons Attribution 4.0 International License.
Read Full License

Additional Declarations: No competing interests reported.

Defect Geometry and Concentration Controlled Excitonic Landscape in Monolayer MX_2-family: A Systematic G_0W_0-BSE Study of Chalcogen Vacancies

Shishir Timilsena[a], Sanju Gupta[b,c,*], Muhammad Idrees Bhatti[a], and Nicholas Dimakis[a,*]
[a]Department of Physics and Astronomy, University of Texas-Rio Grande Valley, Edinburg, TX 78539, USA
[b]Department of Physics, The Pennsylvania State University, University Park, PA 16802, USA
[c]Department of Physics and Astronomy, University of Georgia, Athens, GA 30602, USA

Abstract

Two-dimensional transition metal dichalcogenides (TMDCs) host strongly bound excitons that dominate their optical response, making them promising platforms for optoelectronic and quantum technologies. Native chalcogen vacancies introduce additional excitonic states whose character is highly sensitive to vacancy concentration and geometry. We present a systematic first-principles study that combines G_0W_0 quasiparticle calculations with the Bethe–Salpeter equation (BSE) to investigate excitonic properties in pristine and chalcogen-vacancy-defective monolayers of MoS_2, $MoSe_2$, and WSe_2 across varying vacancy concentrations and geometries. We classify the defect-induced excitons into three types: D_1 (perturbed valence-to-defect), D_2 (shallow defect-to-defect), and Deep D_2 (deeply localized defect-to-defect) transitions. These defect excitons redistribute oscillator strength from the pristine-like excitons toward lower energies, with the extent of redistribution strongly dependent on vacancy concentration and geometry. By combining BSE oscillator strengths, fatband transition weights, and Wannier-interpolated G_0W_0 band structures, we provide microscopic assignments for the defect-related excitons. The theoretical predictions are complemented by room-temperature micro-Raman, photoluminescence, and spectroscopic ellipsometry measurements on exfoliated monolayers. Notably, the low-energy shoulder observed in the photoluminescence spectrum of defective MoS_2 is consistent with additional low-energy optical transitions predicted by the G_0W_0-BSE calculations. These findings establish a framework for engineering excitonic spectra in monolayer TMDCs through the controlled introduction of chalcogen vacancies, with potential relevance to defect-based quantum light emitters for quantum information technologies.

*Corresponding authors: nicholas.dimakis@utrgv.edu, sgup77@gmail.com

1. Introduction

Two-dimensional transition metal dichalcogenides (TMDCs), particularly monolayer MoS_2, $MoSe_2$, and WSe_2, have attracted considerable attention due to their exceptional optoelectronic properties and potential for device applications [1-7]. In the monolayer limit, these materials exhibit direct band gaps and strongly bound excitons with binding energies of approximately 0.3–0.5 eV that dominate their optical response [8,9]. As a result, the optical response of monolayer TMDCs is largely governed by excitonic transitions, making them attractive platforms for optoelectronic devices and quantum photonic applications [10]. However, native point defects—particularly chalcogen vacancies—inevitably perturb the electronic structure and introduce additional excitonic states. The energies and microscopic character of these defect-induced excitons depend sensitively on vacancy concentration and defect geometry. Understanding how vacancy concentration and geometry modify excitonic states is therefore essential for both fundamental studies and the rational design of defect-engineered two-dimensional optoelectronic materials.

Density functional theory (DFT) [11,12] has been widely used to investigate the electronic structure and defect-induced states in pristine and defective TMDC monolayers [13-15]. However, DFT within local-density or generalized-gradient approximations typically underestimates band gaps [16] and cannot accurately describe excitonic effects. Many-body perturbation theory approaches based on the GW approximation combined with the Bethe–Salpeter equation (GW-BSE) are therefore required to obtain reliable quasiparticle energies and excitonic optical spectra [17-19]. While GW-BSE calculations have been successfully applied to pristine TMDC monolayers, most existing studies have focused on individual materials and limited supercell sizes, preventing a systematic understanding of how vacancy concentration, defect geometry, and host material influence defect-induced excitons [20-22]. Mitterreiter *et al*. combined photoluminescence (PL) measurements with GW-BSE calculations to investigate sulfur vacancies in MoS_2 and identified defect-bound excitons [23]. However, their study was restricted to MoS_2 and did not provide a comparative analysis across the broader MX_2 family (M = Mo, W; X = S, Se). To our knowledge, a systematic GW-BSE study addressing these aspects across the MoS_2–$MoSe_2$–WSe_2 family has not yet been reported.

Experimentally, PL spectroscopy is widely used to probe excitonic transitions and defect-related emission in TMDC monolayers [24,25], while Raman spectroscopy provides complementary information on vibrational modes and defect-induced structural disorder [25]. Direct measurements of the quasiparticle gap using time-resolved angle-resolved photoemission spectroscopy (trARPES) and scanning tunneling spectroscopy (STS) are typically limited to substrate-supported monolayers [26]. In such cases, strong dielectric screening can substantially modify the electronic structure relative to freestanding monolayers [17].

In this work, we present a systematic G_0W_0–BSE study of excitonic properties in pristine and chalcogen-vacancy-defective monolayer MoS_2, $MoSe_2$, and WSe_2. Using 1×1, 2×2, and 4×4 supercells, we examine single and double chalcogen vacancies in both same-layer and opposite-layer configurations, with spin–orbit coupling included in selected cases. We systematically analyze how vacancy concentration, defect geometry, and host material govern the formation and evolution of defect-induced excitons. The theoretical results are supported by room-temperature Raman, PL, and spectroscopic ellipsometry measurements on exfoliated TMDC monolayers, including defect-sensitive measurements on MoS_2. This combined theoretical and experimental approach provides a unified framework for identifying and interpreting defect-induced excitons in monolayer TMDCs.

2. Theoretical Framework and Experimental Methods

2.1 Computational methods

2.1.1 Supercell and unit-cell modeling for pristine and defective monolayers. The MoS_2, $MoSe_2$, and WSe_2 monolayers were modeled using the primitive unit cell (1×1) and 2×2 and 4×4 supercells in the $P6_3/mmc$ space group. Fig. 1 shows the atomic structures of pristine and defective monolayers in this work. For each material, we examined the pristine monolayer, a single chalcogen vacancy V_{1X} (X = S or Se), and double chalcogen vacancies in the same-layer (V_{2X}^{s}) and opposite-layer (V_{2X}^{o}). All structures were relaxed by allowing atomic positions to vary while keeping the lattice parameters fixed. This approximation is reasonable because defect-induced changes in the lattice constants are expected to be small [27-30]. The lattice constants used in this work are provided in Table S1 of the Supplementary Materials. A vacuum spacing of at least 12 Å was included in the out-of-plane direction to minimize spurious interactions between periodic images.

2.1.2 Computational parameters. DFT calculations were performed using the projector-augmented wave (PAW) method [31] as implemented in the Vienna *Ab initio* Simulation Package (VASP) [32-35]. The exchange–correlation functional was treated within the generalized gradient approximation (GGA) [36] using the Perdew–Burke–Ernzerhof (PBE) functional [37]. A plane-wave kinetic energy cutoff of 450 eV was used together with GW-compatible PAW potentials.

The PBE electronic structure was refined using exact diagonalization of the Kohn–Sham Hamiltonian, including the large number of unoccupied states required for the subsequent G_0W_0 calculations. Specifically, 224, 840, and 960 bands were used for the 1×1, 2×2, and 4×4 supercells, respectively.

Single-shot G_0W_0 [38] calculations were performed for all configurations to obtain the quasiparticle energies. These energies were then used as input for the BSE calculations [20-22] to obtain dielectric functions, BSE fatbands, and excitonic properties. The BSE calculations were carried out beyond the Tamm–Dancoff approximation (TDA) [39] by including both resonant and anti-resonant contributions to the electron–hole Hamiltonian. In the BSE calculations, we used 20 occupied and 20 unoccupied bands. Coulomb truncation was applied to both G_0W_0 and BSE calculations to minimize interactions between periodic images [40].

The Wannier90 and WannierTools packages were employed to compute the total and projected band structures [41,42]. Brillouin-zone integration was performed using Γ-centered k-point meshes of 16×16×1, 8×8×1, and 4×4×1 for the 1×1, 2×2, and 4×4 supercells, respectively.

Spin–orbit coupling was included in the 1×1 and 2×2 calculations [43]. For the 4×4 supercells, spin–orbit coupling was omitted because fully relativistic G_0W_0–BSE calculations were computationally prohibitive. These calculations were used primarily to assess the effects of supercell size and vacancy concentration. For the defective configurations, BSE fatband representations were calculated for the first 7,000 excitonic states to capture the numerous closely spaced defect-induced and mixed host–defect excitons that appear in these spectra. The excitonic wavefunctions were decomposed into their dominant electron–hole pair contributions (k-point, electron and hole band indices, quasiparticle energies, and transition weights). These data, together with BSE oscillator strengths and Wannier-interpolated G_0W_0 band structures, were used to determine the microscopic character of optically active and mixed host–defect excitons.

2.2 Experimental Methods

Micromechanically exfoliated monolayer MoS_2, $MoSe_2$, and WSe_2 flakes were placed on SiO_2 (~295 nm)/Si substrates. High-resolution resonance Raman spectra were acquired using a commercial micro-Raman spectrometer (InVia Renishaw, UK) equipped with an 1800 g/mm grating and edge filters with a cutoff near 100 cm^{-1}. A 633 nm excitation laser (E_L = 1.92 eV) was used, with the power incident on the sample kept below 100 μW to avoid local heating and thermal degradation. The laser spot size on the sample was approximately 1 μm with the 100× objective lens. The spectral resolution was ~1 cm^{-1}, and spectra were recorded in backscattering geometry over the 100–800 cm^{-1} range for 60–100 s. The laser power measured below the objective was 75 μW for MoS_2 and 68 μW for $MoSe_2$ and WSe_2. All spectra were calibrated against the Si(001) peak at 520.7 cm^{-1}.

Room-temperature micro-PL spectra were measured using a spectrometer (Jobin-Yvon Horiba) equipped with a 532 nm excitation laser (E_L = 2.33 eV). The laser was focused with a 100× objective, yielding a spot size of ~1 μm. The laser power was kept at ≤ 100 μW to avoid photodegradation while maintaining sufficient signal intensity. PL spectra were measured over the 1.2–2.2 eV range with a spectral resolution below 5 meV using a 300 gr/mm grating and an air-cooled CCD detector with an edge filter cutting at approximately 100 cm^{-1}.

Variable-angle spectroscopic ellipsometry (VASE; J. A. Woollam Co., Inc.) was used to determine the refractive index and extinction coefficient. Measurements were performed at an incident angle of 70.09° over the wavelength range 400–1600 nm, following the procedure described in Ref. [44].

3. Results and Discussion

3.1. Raman and PL characterization

Fig. 2 presents representative Raman and room-temperature PL spectra of pristine monolayer MoS_2, $MoSe_2$, and WSe_2, along with spectra from a defective MoS_2 monolayer. Raman and PL spectroscopy were employed to verify the monolayer character of the exfoliated samples and to provide experimental reference data for comparison with the calculated optical properties.

For pristine monolayer MoS_2, the Raman spectra exhibit the characteristic in-plane E_{2g}^1 and out-of-plane A_{1g} modes at 384 and 404 cm^{-1}, respectively, arising from the intralayer S–Mo–

S vibrations. The frequency separation of approximately 18–20 cm^{-1} between these modes confirms the monolayer thickness. The defective MoS_2 spectrum retains the characteristic MoS_2 Raman modes, indicating that the monolayer lattice largely remains preserved despite the presence of defects. Additional intense features above 400 cm^{-1} in MoS_2 are attributed to higher-order modes such as 2LA(M).

For monolayer $MoSe_2$, the A_{1g} mode appears in the 237–239 cm^{-1} range, while the in-plane E^1_{2g} mode is observed near 287.2 cm^{-1}. For WSe_2, the Raman spectrum shows a single dominant peak arising from the nearly degenerate E^1_{2g} and A_{1g} modes, which cannot be clearly resolved under the present measurement conditions. An additional feature near 260 cm^{-1} is assigned to the 2LA(M) mode. The near degeneracy of the E^1_{2g} and A_{1g} modes in monolayer WSe_2 is consistent with previous reports.[45]

For bulk MoS_2, the band gap is indirect. As the material is thinned toward the monolayer limit, the band gap becomes direct at the K point, leading to a strong increase in PL intensity[46]. The PL spectrum of monolayer MoS_2 shows emission peaks near 1.88 eV (670 nm) and 1.98 eV, assigned to the A (X_A) and B (X_B) excitons, respectively. Monolayer $MoSe_2$ exhibits a strong PL peak near 1.57 eV (792 nm), while monolayer WSe_2 shows an emission peak centered near 1.65 eV (752 nm). These measured excitonic transition energies provide experimental reference values for comparison with the calculated optical spectra.

The defective MoS_2 PL spectrum also exhibits a red shifted lower-energy shoulder near 1.81 eV (685 nm), consistent with either defect-bound trion emission or defect-related localized excitonic emission. Although individual defect excitons are not resolved experimentally, this shoulder is consistent with the emergence of additional low-energy optical transitions. This observation is in agreement with the defect-induced excitons predicted by the G_0W_0–BSE calculations.

Spectroscopic ellipsometry was used to determine the real and imaginary parts of the dielectric function of monolayer MoS_2 and WSe_2, as shown in Fig. 3. Measurements were performed over the wavelength range 400–1600 nm. The complex dielectric function was obtained from the ellipsometric parameters Ψ and Δ using standard procedures [47]. In both materials, the high-energy C-exciton resonance is observed in the 2.4–2.8 eV range. For WSe_2, an additional broad feature appears between the B- and C-exciton regions, labeled $X_{A'}/X_{B'}$ to indicate an unresolved higher-energy excitonic transition.

3.2 Electronic and optical properties

3.2.1 Band-structure and density-of-states calculations. Figs. 4 and 5 show the Wannier-interpolated G_0W_0 band structures together with the corresponding G_0W_0 projected densities of states (DOS) for pristine and defective 2×2 supercells of MoS_2, $MoSe_2$, and WSe_2. Results for the 4×4 supercells are shown in Figs. S1 and S2.

For pristine 2×2 supercells with spin–orbit coupling included, the G_0W_0 band gaps are 2.75–2.81 eV for MoS_2 (Fig. 4a,b) and 2.17 eV for both $MoSe_2$ (Fig. 4i,j) and WSe_2 (Fig. 5a,b). These values are in good agreement with previous GW studies [17,19,48-51]. The projected band structures and DOS show that the valence-band maximum is primarily composed of chalcogen p-orbitals hybridized with metal d-orbitals, while the conduction-band minimum is dominated by metal d-character [52]. The smaller band gaps of $MoSe_2$ and WSe_2 relative to MoS2 arise from the larger atomic size and lower electronegativity of Se, which weakens the chalcogen-p/metal-d hybridization.

Chalcogen vacancies substantially modify the electronic structures by introducing defect-derived states within or near the pristine band gap. These states originate mainly from the d-orbitals of under-coordinated metal atoms surrounding the vacancy. In the 2×2 supercells, the higher vacancy concentration leads to stronger vacancy–vacancy and vacancy–host interactions, resulting in dispersive defect-derived bands that hybridize with the host valence states (Figs. 4c–h, k–p and 5c–h). In contrast, the reduced interaction between periodic defect images in the 4×4 supercells leads to flatter bands and more localized defect states (Figs. S1c−h, k−p and S2c−h). These findings are consistent with previous reports on defective MoS_2 and $MoSe_2$ monolayers [52,53].

Some vacancy configurations produce indirect band gaps, such as MoS_2 V_{1S} and V_{2S}^{o}. The direct–indirect gap character depends on both the vacancy number and vacancy geometry, which modify defect–defect coupling and defect–host hybridization. Although increasing the vacancy concentration generally reduces the band gap, several WSe_2 configurations deviate from this trend. In defective WSe_2, the strong W-5d character of the band-edge states allows Se-vacancy-derived states to redistribute within the gap without producing a monotonic decrease in the band-edge separation. Notably, the WSe_2 4×4 opposite-layer divacancy exhibits a larger-than-expected band gap because weaker vacancy–vacancy coupling between opposite chalcogen layers produces more localized defect states. Overall, the quasiparticle band structures demonstrate that vacancy

concentration, vacancy geometry, and host material collectively govern the localization and energetic position of defect-derived states in these TMDC monolayers.

3.2.2 Dielectric function calculations

Tables 1–3 summarize the G_0W_0 direct band gaps (E_g^{GW}), exciton binding energies (E_b), and optical transition energies for pristine and defective MoS_2, $MoSe_2$, and WSe_2 configurations. The exciton binding energy is defined as $E_b = E_g^{GW} - E_{optical}^{BSE}$, where E_g^{GW} is the GW-calculated quasiparticle direct band gap and $E_{optical}^{BSE}$ is the lowest bright optical transition energy obtained from the BSE. Larger E_b values correspond to stronger electron–hole interactions and reduced dielectric screening [54].

Fig. 6 shows the in-plane component of the imaginary part of the dielectric function averaged over the x and y directions, $(\mathrm{Im}\,\varepsilon_x + \mathrm{Im}\,\varepsilon_y)/2$, for the pristine and defective 2×2 supercells. The spectra were calculated using the full BSE, the random-phase approximation (RPA), and the independent-particle approximation (IPA) [55]. The corresponding out-of-plane component, $\mathrm{Im}\,\varepsilon_z$, appears at much higher energies and is not considered here [56]. Fig. 6 also shows the exciton positions for the pristine configurations and the assigned defect-related excitonic features for the defective configurations. The corresponding 4×4 spectra and exciton assignments are shown in Fig. S3.

Comparison of the IPA, RPA, and BSE spectra allows the separate effects of quasiparticle corrections and electron–hole interactions on the optical response to be distinguished. Whereas the IPA spectra are derived from DFT eigenvalues and the RPA spectra are based on G_0W_0 quasiparticle energies, the full BSE additionally includes electron–hole interactions. Consequently, the BSE spectra exhibit a redshift of the absorption onset and a redistribution of spectral weight relative to the IPA and RPA spectra [57,58]. For the pristine MoS_2, $MoSe_2$, and WSe_2 monolayers, the BSE optical gaps closely follow the trends observed in the G_0W_0 quasiparticle band gaps, indicating that the optical response is primarily governed by the underlying pristine electronic structure.

3.2.3 Pristine excitons and supercell-size effects

We now examine the excitonic features of pristine MoS_2, $MoSe_2$, and WSe_2. The A (X_A) and B (X_B) excitons arise from direct K/K′-valley transitions from the upper and lower spin–orbit-split valence bands, respectively, to the conduction-band minimum. The corresponding K and K′ excitons are valley-degenerate by time-reversal symmetry [17]. The higher-energy A′ ($X_{A'}$) and B′ ($X_{B'}$) excitons correspond to Rydberg-like excited states of the A and B excitonic series. In contrast, the C exciton originates from multiple transitions involving the top valence band and higher-lying conduction bands over extended regions of the Brillouin zone, producing a broad spectral feature associated with an enhanced joint density of states [17]. Higher Rydberg-like 3s/3p states are identified for the pristine 2×2 and 4×4 supercells of $MoSe_2$ and WSe_2, as well as in selected defect configurations (Tables 1–2). Although the supercell k-point meshes provide equivalent effective sampling of the primitive Brillouin zone, the larger 2×2 and 4×4 supercells allow assessment of finite-size effects and provide additional insight into the localization characteristics of higher-lying excitonic states [54].

Table 1 shows good agreement between the present pristine-exciton energies and previous experimental and computational reports. For MoS_2, Qiu *et al.* used Quantum ESPRESSO[59] with the BerkeleyGW code[60] on a dense 72×72×1 Brillouin-zone grid to calculate excitons in the primitive unit cell, resolving the A, B, A′, and B′ excitons.[17] Their A- and B-exciton energies are in close agreement with the experimental values (Table 1). In contrast, earlier VASP-based calculations by Ramasubramaniam used a coarser 6×6×1 grid, which may limit the convergence of higher excitonic states and exciton binding energies [18]. Since exciton binding energies in two-dimensional materials are highly sensitive to Brillouin-zone sampling, coarse k-point meshes may lead to enhanced exciton localization and overestimated binding energies. The experimental transition energies measured in this work are also consistent with previous reports.

For pristine configurations with spin–orbit coupling included, the A-exciton binding energy follows the trend MoS_2 > $MoSe_2$ > WSe_2 (Table 1). This decrease is consistent with enhanced dielectric screening from the more spatially extended and polarizable Se-p and W-5d orbitals, which weaken the electron–hole interaction. Because spin–orbit coupling was not included in the 4×4 calculations, these results are discussed separately.

For pristine MoS_2, our G_0W_0-BSE calculations place the A and B excitons at 2.10 and 2.25 eV, respectively, giving a spin–orbit-induced splitting of 0.15 eV. The A–B separation increases in the order WSe_2 > $MoSe_2$ > MoS_2, reflecting the stronger spin–orbit coupling of heavier chalcogen and transition-metal atoms, particularly the W-dominated valence-band states in WSe_2. The calculated pristine MoS_2 A and B exciton energies are blue-shifted relative to some previous calculations and experimental absorption and PL measurements. This shift can be attributed to differences in computational parameters, including k-point sampling, dielectric screening, and convergence levels in the GW and BSE calculations. The higher-energy A′, B′, and C features are also resolved and remain consistent with prior theoretical reports. For the larger pristine MoS_2 supercells, modest shifts in the excitonic features are observed. In the 2×2 case, the A–C excitons are slightly blue-shifted. These differences suggest that residual finite-size effects and the spatial extent of the excitonic wave functions may influence the calculated excitonic properties despite maintaining equivalent effective Brillouin-zone sampling.

For pristine MoS_2, the 4×4 calculations show that the higher-energy excitonic features remain within a similar energy range to those obtained for the smaller supercells. Larger deviations are observed for $MoSe_2$ and especially for WSe_2, reflecting the increased importance of spin–orbit coupling, which was omitted in the 4×4 calculations due to computational cost.

3.2.4 Defect-induced excitons

Tables 2 and 3 summarize the main excitonic features of the defective 2×2 and 4×4 supercells, respectively. The complete energy ranges and full peak assignments are provided in Tables S2 and S3. The calculated optical spectra are classified into three physically distinct defect-induced excitonic features: Deep D_2, D_2, and D_1. Both the Deep D_2 and D_2 excitons arise from defect-to-defect transitions, with holes and electrons residing in occupied and unoccupied defect-derived states, respectively. The D_2 excitons involve relatively shallow defect-derived states near the valence-band maximum, whereas the Deep D_2 excitons involve deeper and more localized defect-derived states located farther below the valence-band maximum. In contrast, the D_1 excitons correspond to transitions from the perturbed valence-band manifold to defect-derived states in the conduction-band region. In addition to these defect-induced excitons, perturbed host-like A, B, A′, B′, C, and higher-order Rydberg-like features may also be resolved

in the defective configurations. This classification scheme is used analogously to the D_1 and D_2 defect excitons reported for chalcogen vacancies in monolayer MoS_2 by Mitterreiter *et al.* [23].

In defective configurations, the presence of multiple defect-induced peaks and overlapping excitonic features makes the identification and assignment of individual excitons challenging. Therefore, defect-induced and perturbed host-like excitons are assigned by combining BSE oscillator strengths, BSE fatband transition weights, and Wannier-interpolated G_0W_0 band structures. The oscillator strengths identify optically relevant excitons, whereas the Wannier-interpolated band structures reveal the perturbed valence- and conduction-band edges and the defect-derived states. The BSE fatband output then provides the dominant electron–hole contributions to each exciton, including the k-point location, hole and electron bands, and transition weight. For all defective configurations, optically active defect-induced excitons appear below the pristine A-exciton region, redistributing oscillator strength toward lower photon energies in both the 2×2 and 4×4 supercells. This redistribution is stronger for the 2×2 configurations, consistent with the higher vacancy concentration and stronger vacancy–vacancy and vacancy–host interactions in the smaller supercells (Fig. 6, Figs. S3, and Tables 2–3). This behavior is consistent with the G_0W_0 band structures, where vacancy-derived states reduce the effective quasiparticle transition energies by introducing additional electronic states within or near the pristine band gap. This theoretical redshift is consistent with the experimentally observed lower-energy shoulder in the PL spectrum of defective MoS_2. While the individual D_1 and D_2 excitons are not resolved experimentally, the calculations indicate that the additional low-energy emission is associated with vacancy-induced excitonic states.

We start our analysis with the MoS_2 single S-vacancy configuration, V_{1S}, comparing the 2×2 and 4×4 supercells. In the 2×2 supercell, the defect-induced excitons are strongly redshifted relative to the pristine A-exciton region, with intense D_1 transitions appearing at about 1.13–1.30 eV. These low-energy D_1 transitions have large oscillator strengths, indicating substantial redistribution of optical spectral weight into defect-induced excitons. Higher-energy D_2 and Deep D_2 features also appear, whereas perturbed host-like A–C excitons remain resolved (Tables 2 and S2). In the 4×4 supercell, the first optically active D_1 excitons occur at higher energies, near 1.64 eV, and with smaller oscillator strengths than in the 2×2 case (Tables 3 and S3). The strongest defect-induced features are mixed D_2/A′-like transitions near 2.45–2.46 eV, as indicated by the

dominant BSE transition weights (Fig. S3b). Overall, the higher vacancy concentration in the 2×2 supercell produces stronger defect–host and defect–defect interactions, leading to a larger redshift and stronger fragmentation of the optical spectrum, whereas the 4×4 supercell shows more clearly separated defect-induced and host-like excitonic features.

We next consider the MoS_2 divacancy configurations, comparing same-layer V_{2S}^{S} and opposite-layer V_{2S}^{O} vacancies in the 2×2 and 4×4 supercells. For both geometries, the excitonic spectrum is redshifted relative to the single-vacancy configuration, with the effect more pronounced for V_{2S}^{S} and for the 2×2 supercells. In contrast to V_{1S}, where the low-energy defect-induced spectrum is dominated by D_1 transitions, the same-layer divacancy V_{2S}^{S} exhibits intense D_2 transitions at very low energies (e.g., 0.27–0.42 eV in the 2×2 supercell, Fig. 6c) with very large oscillator strengths. This change in character arises from the presence of vacancy-derived states in both the valence- and conduction-band regions near the Fermi level, which reduces the effective quasiparticle transition energies and favors optically active defect-to-defect D_2 transitions. For the same supercell size, the D_2 excitons are less intense in the opposite-layer V_{2S}^{O} configuration, indicating weaker defect–defect coupling and a smaller redistribution of optical spectral weight into low-energy defect-induced excitons. Overall, the comparison shows that the divacancy excitonic response is controlled not only by vacancy number, but also by vacancy geometry and the resulting defect–defect coupling.

The Se-vacancy systems show material-dependent deviations from the MoS_2 trends. In the 2×2 single-vacancy configurations, $MoSe_2$ behaves similarly to MoS_2: the perturbed A- and B-like excitons are shifted to higher energies relative to the pristine case, while the A′-like feature is redshifted and lies between the A and B excitons. In WSe_2, the single Se vacancy produces a weaker perturbation, with the perturbed A-like exciton remaining close to the pristine A-exciton energy, while the higher-energy B/A′ region is shifted to lower energies. For the $MoSe_2$ and WSe_2 divacancies, the dominant defect-exciton character varies with vacancy geometry and supercell size. $MoSe_2$ switches between D_1, D_2, and mixed D_1/D_2 features depending on the divacancy arrangement, whereas WSe_2 remains mostly D_1-dominated, except for the 2×2 same-layer divacancy, where mixed D_1/D_2 character is observed.

3.2.5 BSE fatband analysis

The BSE fatband analysis provides a direct visualization of the electron–hole character of representative excitons on the Wannier-interpolated GW band structures. Fig. 7 shows Wannier-interpolated G_0W_0 band structures overlaid with BSE fatband weights for 2×2 MoS_2 monolayers. Although only the MoS_2 cases are shown here as representative examples, the same analysis was performed for all defective configurations. Larger circles correspond to larger BSE transition weights [61].

For pristine MoS_2, the dominant hole and electron weights are concentrated near the K/K′ valley band-edge states, consistent with the A/B excitons arising from direct band-edge transitions. In contrast, the defective systems exhibit a redistribution of the BSE weights toward vacancy-derived states within the quasiparticle gap and near the band edges. For the single-vacancy configuration, the electron and hole weights are distributed over several defect-derived and perturbed host states, indicating that the first bright exciton has mixed defect–host character. For the same-layer divacancy, the weights are concentrated in only a few dominant transitions, consistent with the large oscillator strength and strong low-energy D_2 character observed in the optical spectrum. For the opposite-layer divacancy, the weights are more broadly distributed over multiple bands and k-points, reflecting weaker defect–defect coupling and stronger mixing between defect-induced and perturbed host-like states.

Overall, the BSE fatband representation illustrates how the dominant electron–hole contributions evolve from pristine band-edge transitions to mixed host–defect and defect-to-defect excitons in defective MoS_2.

4. Conclusion

We performed G_0W_0-BSE calculations to investigate how chalcogen vacancies modify the quasiparticle electronic structure and excitonic spectra of monolayer MoS_2, $MoSe_2$, and WSe_2. Using supercells of varying sizes, we examined single and double vacancies in both same-layer and opposite-layer configurations. The pristine systems reproduce the expected A, B, A′, B′, and C excitonic features with optical trends supported by PL and ellipsometry measurements. Chalcogen vacancies introduce defect-derived states within or near the pristine band gap,

generating optically active defect-induced excitons (D_1, D_2, and Deep D_2) below the pristine A-exciton region and redistributing oscillator strength toward lower energies.

The defect-induced excitonic response depends strongly on vacancy concentration and geometry. The 2×2 supercells show stronger redshifts and greater spectral fragmentation than the 4×4 supercells because of stronger vacancy–vacancy and vacancy–host interactions. Same-layer divacancies, especially in MoS_2, produce intense low-energy D_2 excitons, whereas opposite-layer divacancies generally show weaker defect–defect coupling and more mixed defect–host character. BSE fatband analysis indicates that the redshifted optical features originate from vacancy-induced electronic states. Although individual D_1 and D_2 excitons are not resolved experimentally, the lower-energy shoulder observed in the PL spectrum of defective MoS_2 is consistent with the calculated redistribution of oscillator strength into defect-induced excitonic states.

Overall, these results demonstrate that vacancy type, concentration, and geometry offer effective routes to tailoring excitonic spectra in monolayer TMDCs, with potential implications for defect-engineered optoelectronic devices and defect-based single-photon emitters in quantum information science.

Acknowledgments

The authors thank the Texas Advanced Computing Center (TACC) at The University of Texas at Austin for providing High-Performance Computing (HPC) resources that contributed to the results reported in this work. The author (S.G.) thanks the Department of Physics and Dean's office of research (University of Georgia) as well as University of Central Florida.

Author Contributions

Shishir Timilsena: Data curation, Formal analysis, Investigation, Methodology, Validation, Writing – original draft, Writing – review & editing. **Sanju Gupta:** Conceptualization, Data curation, Methodology, Project administration, Resources, Validation, Writing – original draft, Writing – review & editing. **Muhammad I. Bhatti:** Methodology, Research, and Formal Analysis, Reviewing, and Revising the draft. **Nicholas Dimakis:** Conceptualization, Data curation, Formal analysis, Investigation, Methodology, Project administration, Resources, Supervision, Validation, Writing – original draft, Writing – review & editing.

Data Availability

The data supporting the findings of this study are available from the corresponding authors upon reasonable request. Processed datasets and selected computational outputs will be deposited in a public repository upon acceptance.

Funding

S.T. declares no relevant funding. S.G. discloses support for the research reported in this work from the DEC-37/2022/IDUB/1.1/NOBELIUM IDUB Nobelium Program. M.I.B. and N.D. declare no relevant funding.

Figures and Captions

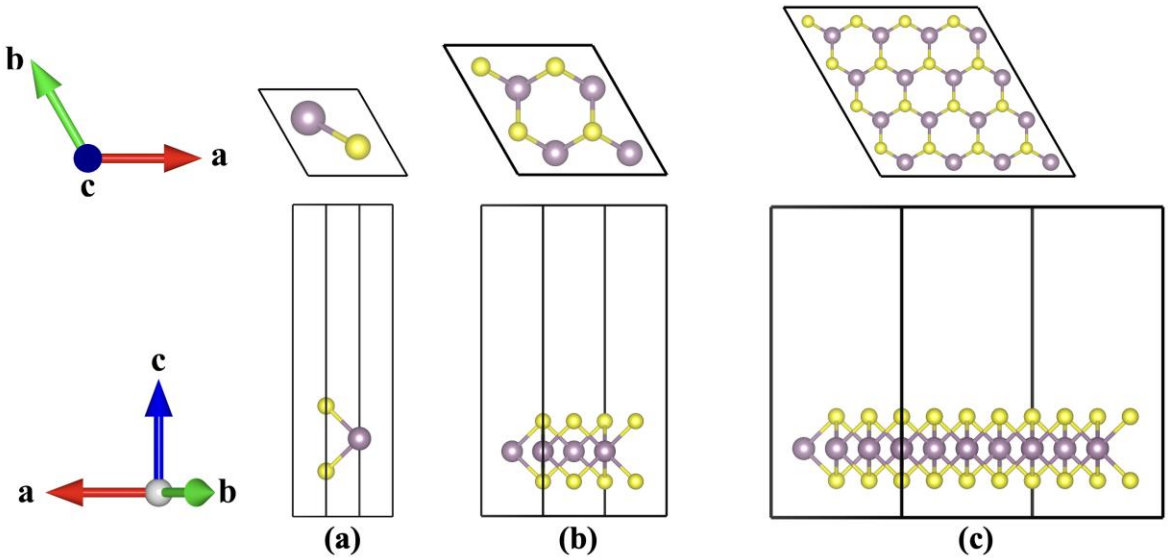


Fig. 1. Top and side views of monolayer MX_2 (M = Mo, W; X = S, Se): (a) primitive unit cell (1×1), (b) 2×2 supercell, and (c) 4×4 supercell. The outlined boxes denote the periodic simulation cells defined by the lattice vectors. Atoms are color-coded: purple for transition-metal atoms (Mo or W) and yellow for chalcogen atoms (S or Se).

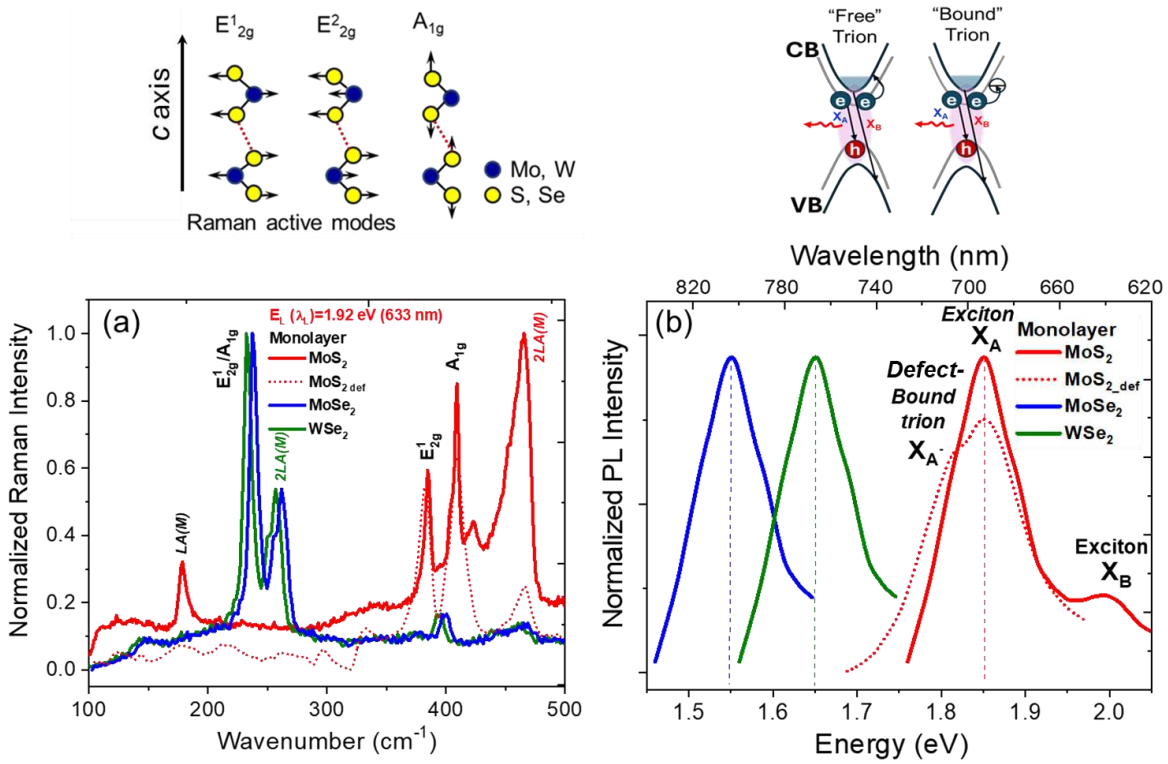


Fig. 2. (a) Raman spectra of monolayer MoS_2, $MoSe_2$, and WSe_2 together with schematic representations of the Raman-active phonon modes. (b) Room-temperature photoluminescence spectra of the same monolayers. A defective MoS_2 spectrum is included to illustrate the appearance of a lower-energy shoulder, consistent with defect-bound trion emission or defect-related localized excitonic emission.

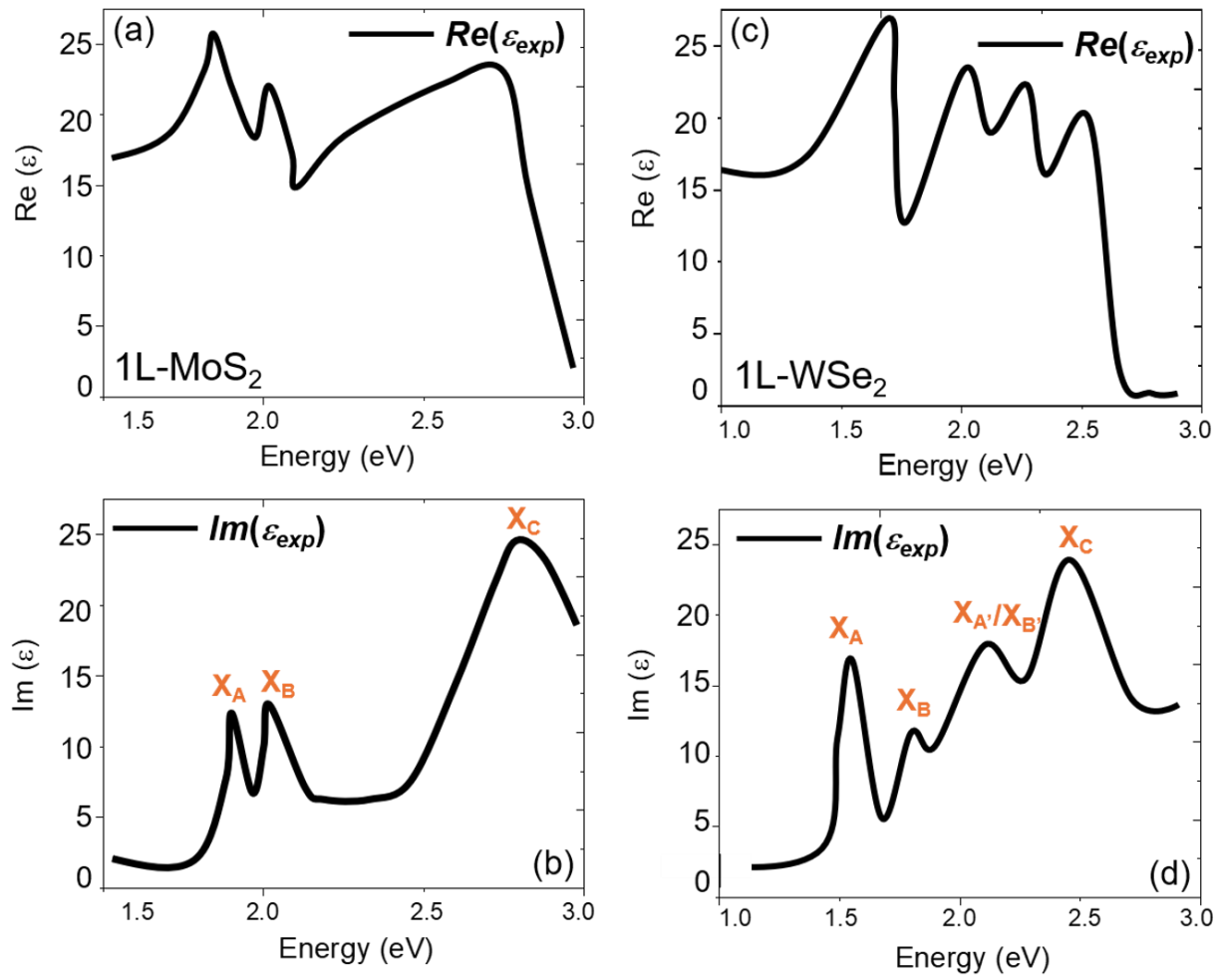


Fig. 3. Experimental real $Re(\varepsilon_{exp})$ and imaginary $Im(\varepsilon_{exp})$ parts of the dielectric function for pristine monolayer MoS_2 and WSe_2 obtained from spectroscopic ellipsometry. Panels (a) and (b) correspond to the real and imaginary parts of the dielectric function for monolayer MoS_2, respectively, whereas panels (c) and (d) show the corresponding real and imaginary parts for monolayer WSe_2, respectively. The labeled features indicate excitonic resonances assigned from the imaginary dielectric response. The $X_{A'}/X_{B'}$ label in WSe_2 denotes an unresolved higher-energy excitonic feature with overlapping higher-order $X_{A'}$- and $X_{B'}$-excitonic contributions.

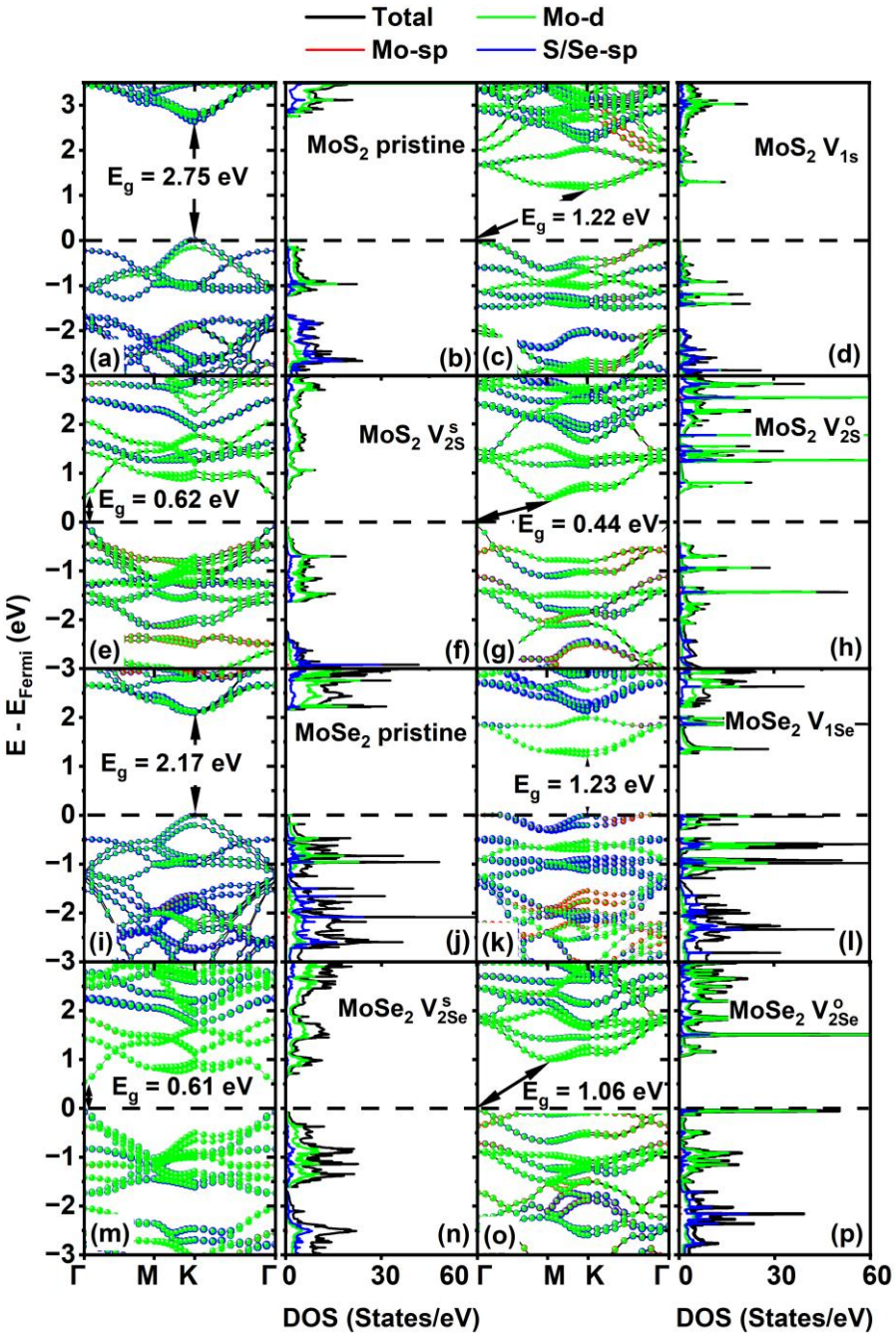


Fig. 4. Wannier-interpolated G_0W_0 band structures and corresponding G_0W_0 density of states (DOS), including both total and orbital-projected contributions, for pristine and defective 2×2 MoS_2 and $MoSe_2$ monolayers with spin–orbit coupling. Panels show (a, b) pristine MoS_2, (c, d) MoS_2 V_{1S}, (e, f) MoS_2 V_{2S}^{s}, (g, h) MoS_2 V_{2S}^{o}, (i, j) pristine $MoSe_2$, (k, l) $MoSe_2$ V_{1Se}, (m, n) $MoSe_2$ V_{2Se}^{s}, and (o, p) $MoSe_2$ V_{2Se}^{o}. Black, red, green, and blue denote the total, metal-sp, metal-d, and S/Se-sp contributions, respectively. The arrows indicate the G_0W_0 band gaps, and the Fermi energy is set to zero. Here, V_{1X}, V_{2X}^{s}, and V_{2X}^{o}, denote a single chalcogen vacancy, two chalcogen vacancies in the same layer, and two chalcogen vacancies in opposite layers, respectively, where X = S or Se.

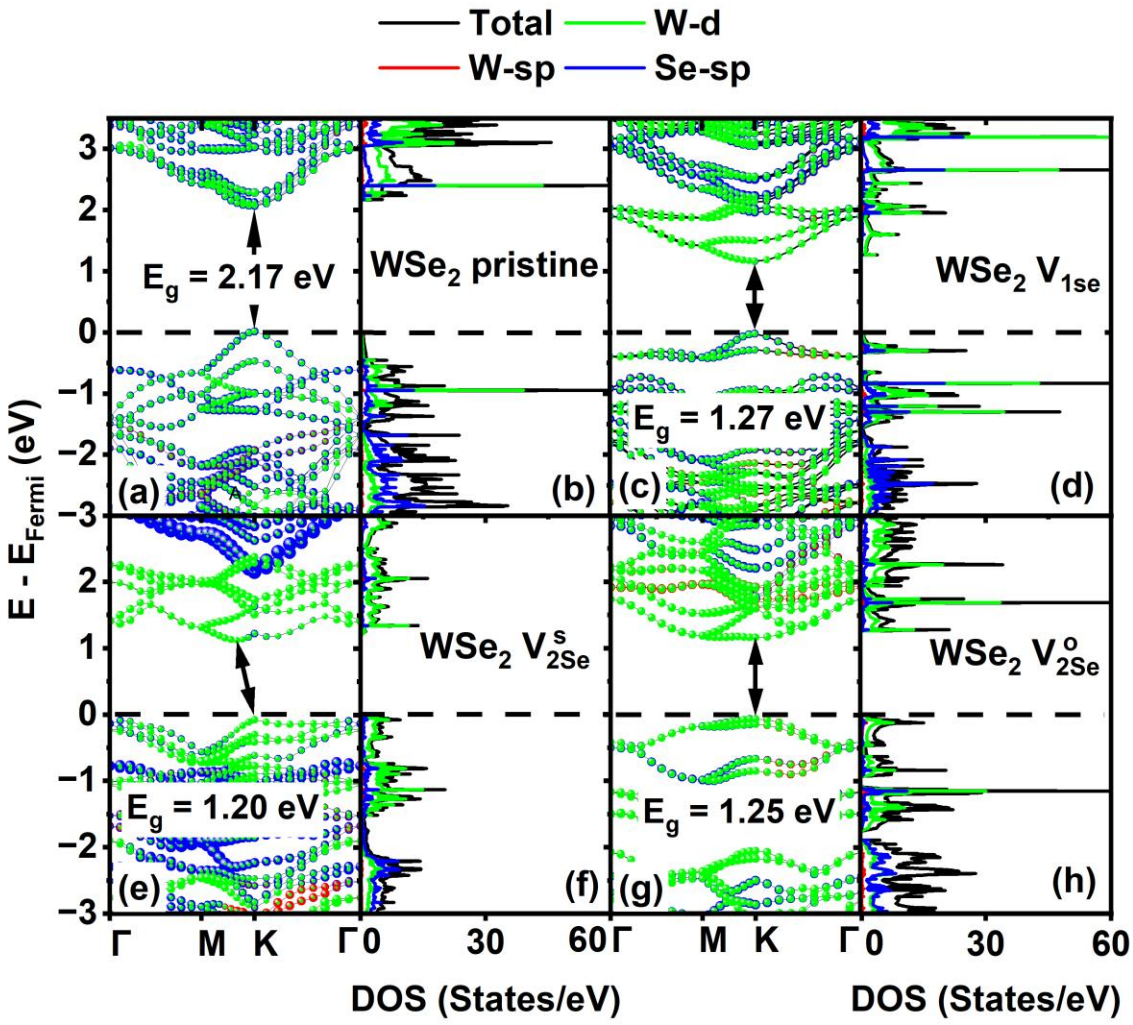


Fig. 5. Wannier-interpolated G_0W_0 band structures and corresponding G_0W_0 density of states (DOS), including both total and orbital-projected contributions, for pristine and defective 2×2 WSe_2 monolayers with spin-orbit coupling. Panels show (a, b) pristine WSe_2, (c, d) single Se vacancy V_{1Se}, (e, f) same-layer Se divacancy V_{2Se}^{s} , and (g, h) opposite-layer Se divacancy V_{2Se}^{o}. Black, red, green, and blue denote total, W-sp, W-d, and Se-sp contributions, respectively. The arrows indicate the G_0W_0 band gaps, and the Fermi energy is set to zero.

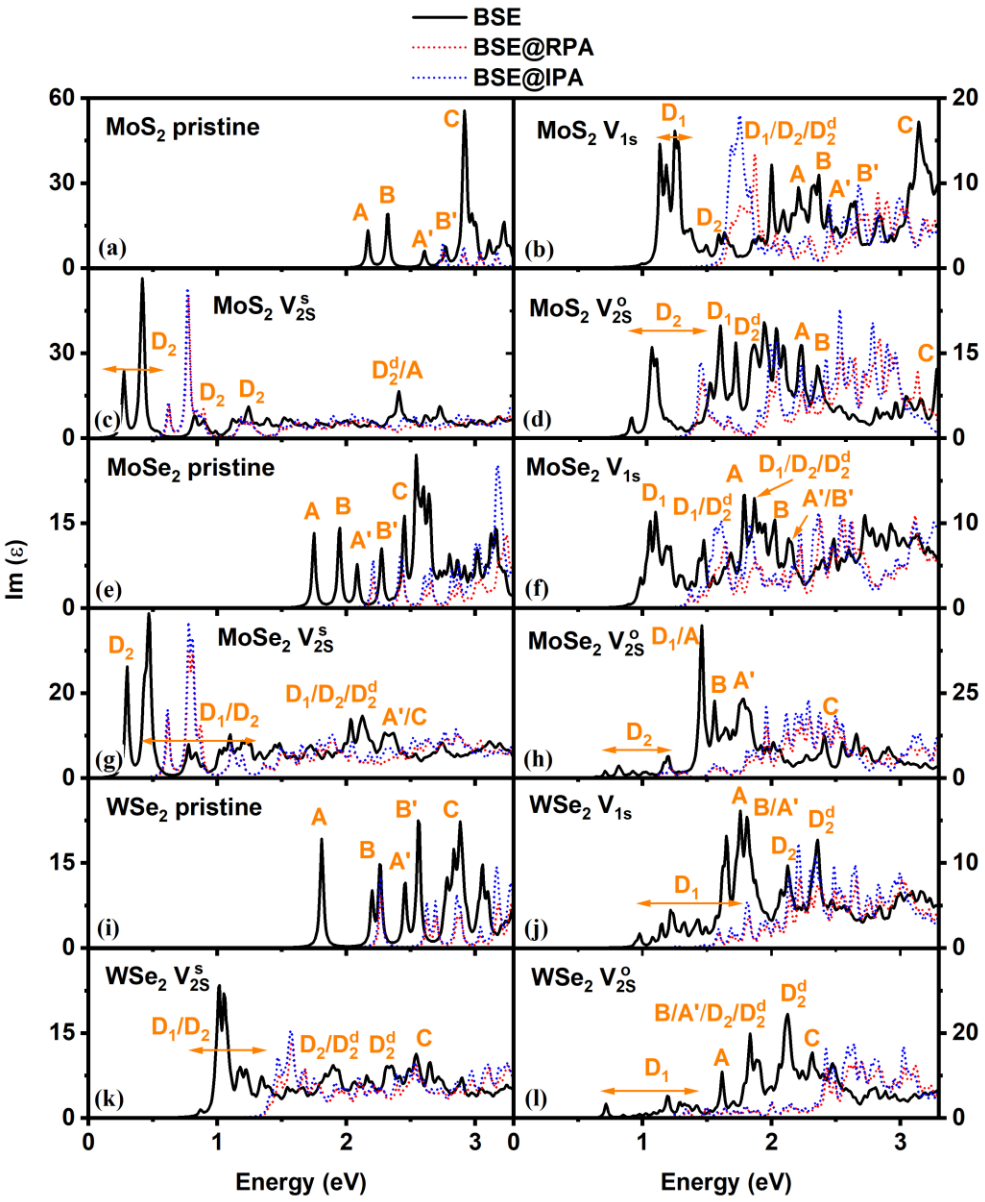


Fig. 6. In-plane component of the imaginary part of the dielectric function calculated for the 2×2 supercells of (a)-(d) MoS_2, (e)-(h) $MoSe_2$, and (i)-(l) WSe_2 monolayers. Panels show (a, e, i) pristine monolayers, (b, f, j) single chalcogen vacancy V_{1X}, double chalcogen vacancies on the same layer (c, g, k) V_{2X}^{S} and (d,h,l) on opposite layers V_{2X}^{o}, where X = S or Se. Black, red, and blue curves correspond to the full BSE, BSE@RPA, and BSE@IPA spectra, respectively. RPA denotes the random-phase approximation, and IPA the independent-particle approximation. The labels A, B, A′, B′, and C denote bright, pristine-like excitonic features, whereas in defective spectra, these labels refer to perturbed, host-like excitons when they remain resolved. Orange arrows in the defective spectra indicate the classified optical regions: D_2^d or Deep D_2 corresponding to deep in-gap defect-to-defect transitions, D_2 corresponding to shallower defect-to-defect transitions, and D_1 corresponding to transitions from perturbed valence-band states to defect-derived states in the conduction band.

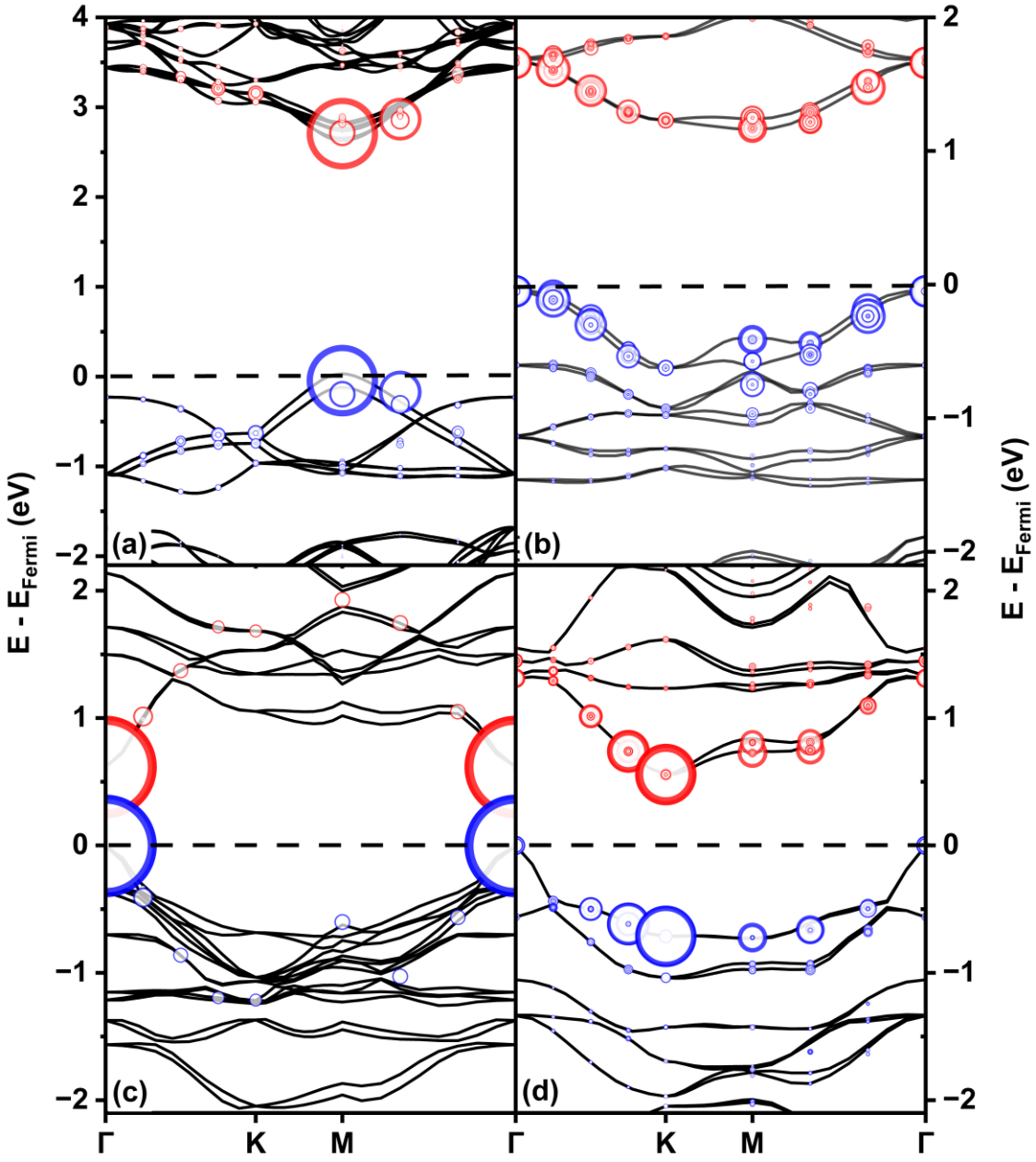


Fig. 7. Wannier-interpolated G_0W_0 band structures overlaid with BSE fat band weights for the representative bright excitonic state of 2×2 MoS_2 monolayers. Panels show (a) pristine MoS_2, (b) single S vacancy V_{1S}, (c) double S vacancy on the same layer V_{2S}^{s}, and (d) on opposite layers V_{2S}^{o}. The black lines represent the Wannier-interpolated G_0W_0 band structures, while the red and blue circles indicate the BSE fat band weights associated with electron and hole contributions, respectively. The circle radii are proportional to the corresponding BSE transition weights. For panel (c), the circle radii are scaled down by a factor of 6 relative to the other panels for clarity. The Fermi energy is set to zero and indicated by the dashed horizontal line.

Table 1. G_0W_0 direct band gap (E_g^{GW}), exciton binding energy (E_b), and energies of five optical transitions (X_A, X_B, X_A', X_B', X_C) obtained from BSE calculations for pristine MoS_2, $MoSe_2$, and WSe_2 monolayers in the 1×1, 2×2, and 4×4 supercell configurations. The 1×1 and 2×2 calculations include spin–orbit coupling. Literature values are included for comparison.

Supercell	Method	E_g^{GW}	E_b	Optical Transition Energies (eV)				
				X_A	X_B	X_A'	X_B'	X_C
MoS_2								
1×1	G_0W_0-BSE (this work)	2.84	0.74	2.10	2.25	2.53	2.70	2.85
	G_1W_0-BSE [17]	2.84[a]	0.96[b]	1.88[b]	2.02[b]	2.20[b]	2.32[b]	2.54[b]
	G_0W_0-BSE [18]	2.82	1.04	1.78	1.96			
	Exp. (this work)			1.85–1.90	1.94–2.03			2.75–2.85
	Exp. (Lit.)			1.85 [62]; 1.88 [63]	1.98 [62]; 2.03 [63]			
2×2	G_0W_0-BSE (this work)	2.75	0.58	2.17	2.32	2.61	2.77	2.91
4×4	G_0W_0-BSE (this work)	2.81	0.71	2.10		2.47; 2.70[d]		2.82
$MoSe_2$								
1×1	G_0W_0-BSE (this work)	2.17	0.43	1.74	1.94	2.08	2.27	2.53
	G_0W_0-BSE [18]	2.41	0.91	1.50	1.75			
	Exp. (this work)			1.56				
	Exp. (Lit.)			1.65[64];1.66 [65]; 1.58[66]	1.87[65]	2.25 [65]	2.45[65]	2.65[65] ;2.71–2.81[66]
2×2	G_0W_0-BSE (this work)	2.17	0.42	1.75	1.95	2.09	2.27; 2.45[d]	2.54
4×4	G_0W_0-BSE (this work)	2.45	0.65	1.81		2.12; 2.30[d]		2.56
WSe_2								
1×1	G_0W_0-BSE (this work)	2.15	0.34	1.81	2.21	2.27	2.47-2.48	2.80
	G_0W_0-BSE [18]	2.42	0.90	1.52	2.00			
	Exp. (this work)			1.55–1.67	1.75–1.85			2.1–2.5
	Exp. (Lit.)			1.73 [67]				
2×2	G_0W_0-BSE (this work)	2.17	0.35	1.81	2.20	2.26	2.45; 2.56[d]	2.88
4×4	G_0W_0-BSE (this work)	2.68	0.68	2.06		2.46; 2.69[d]		2.80

[a] 12×12×1 BZ; [b] 72×72×1 BZ; [c] 6×6×1 BZ; [d] 3s/3p Rydberg state.

Table 2. Direct G_0W_0 band gap (E_g^{GW}), exciton binding energy (E_b), representative prominent defect-related optical peaks selected based on oscillator strength, and perturbed host-like excitonic features for defective 2×2 supercells of MoS_2, $MoSe_2$, and WSe_2 monolayers with spin–orbit coupling. D_1 denotes perturbed valence-to-defect band transitions, D_2 denotes defect-to-defect band transitions involving shallow defect states, and Deep D_2 denotes defect-to-defect transitions involving deeper vacancy-derived states. V_{1X}, V_{2X}^{s}, and V_{2X}^{o} denote a single chalcogen vacancy, same-layer chalcogen divacancy, and opposite-layer chalcogen divacancy, respectively, where X = S or Se. Complete energy ranges and full peak assignments are provided in Table S2.

Defect	E_g^{GW}	E_b	Optical Transition Energies (eV)	
			Main defect-related peaks	**Perturbed host-like features**
			MoS_2	
V_{1S}	1.56	0.57	D_1: 1.13–1.50; mixed D_1/D_2/Deep D_2: 2.00; Deep D_2: 2.31; D_2: 2.09	2.21–2.25[a]; 2.36[b]; 2.44[c]; 2.65[d]; 3.14[e]
V_{2S}^{s}	0.62	0.36	D_1: 0.90; 1.17; 1.38; Deep D_2: 2.42; D_2: 0.27–0.42; 0.79–0.86; 1.12; 1.24	2.41[a]; 2.62 [c]
V_{2S}^{o}	1.27	0.51	D_1: 1.46; 1.68–1.70, 1.77, 1.86, 1.90; Deep D_2: 1.57, 1.72, 1.77, 1.85, 2.56; D_2: 0.83–1.35	2.02[a]; 2.13[b]; 2.98[e]
			$MoSe_2$	
V_{1Se}	1.23	0.34	D_1: 0.98–1.48, 1.78, 1.87; Deep D_2: 1.48, 1.87; D_2: 1.95	1.79 [a], 2.00[c]; 2.08[f]; 2.13[b]; 2.15 [f]
V_{2Se}^{s}	0.61	0.33	D_1: 1.02, 1.05, 1.23; Mixed D_1/D_2: 0.43–0.90; mixed Deep D_2 /D_2: 1.10; Deep D_2: 2.05; D_2: 0.30	2.34[c,e]
V_{2Se}^{o}	1.13	0.49	D_1: 1.44, 1.46, 1.56; D_2: 0.71–1.20	1.46–1.47 [a]; 1.54–1.55[b]; 1.64–1.86 [c]
			WSe_2	
V_{1Se}	1.27	0.32	D_1: 1.21, 1.65–1.66, 1.72; 1.85; Deep D_2: 2.36; D_2: 1.63; 1.76; 1.82; 1.88	1.77–1.79[a]; 1.81[b]; 1.84[c]
V_{2Se}^{s}	1.30	0.43	Mixed D_1/D_2: 0.99–1.21; Deep D_2:1.84; D_2: 1.34, 1.54	2.56[e]
V_{2Se}^{o}	1.25	0.53	D_1: 1.20; mixed Deep D_2/D_2: 1.83; Deep D_2: 1.88, 2.10, 2.13; D_2: 1.90, 2.06	1.62[a]; 1.79–1.84[b]; 1.87–1.91[c]; 2.31[e]

Perturbed host-like features are labeled as follows: [a] A-like; [b] B-like; [c] A′-like; [d] B′-like; [e] higher-lying mixed/C-like; [f] 3s/3p Rydberg state.

Table 3. Direct G_0W_0 band gap (E_g^{GW}), exciton binding energy (E_b), representative prominent defect-related optical peaks selected based on oscillator strength, and perturbed host-like excitonic features for defective 4×4 supercells of MoS_2, $MoSe_2$, and WSe_2 monolayers without spin–orbit coupling. D_1 denotes perturbed valence-to-defect band transitions, D_2 denotes defect-to-defect band transitions involving shallow defect states, and Deep D_2 denotes defect-to-defect transitions involving deeper vacancy-derived states. V_{1X}, V_{2X}^{s}, and V_{2X}^{o} denote a single chalcogen vacancy, same-layer chalcogen divacancy, and opposite-layer chalcogen divacancy, respectively, where X = S or Se. Complete energy ranges and full peak assignments are provided in Table S3.

Defect	E_g^{GW}	E_b	Optical Transition Energies (eV)	
			Main defect-related peaks	**Perturbed host-like features**
			MoS_2	
V_{1S}	2.14	0.72	D_1: 1.64; mixed D_1/D_2: 1.76; D_2: 1.93–2.46	2.46[i]; 2.73[c]
V_{2S}^{s}	1.81	0.68	D_1: 1.78, 1.80; mixed D_1/D_2: 1.79; Deep D_2: 2.24; D_2: 1.14–1.20, 1.84	2.29–2.31[ii]; 2.56[c]
V_{2S}^{o}	2.06	0.77	D_1: 1.45; D_2: 1.96	1.95[iii]; 2.13[b]; ≥2.21[c]
			$MoSe_2$	
V_{1Se}	2.14	0.71	D_1: 1.43; mixed D_1/D_2: 1.55; D_2: 2.24	2.25[i]; 2.53[b]; 2.51[c]
V_{2Se}^{s}	1.93	0.65	D_1: 2.04; D_2: 1.28–1.83	2.05 [iv]; 2.19[v]; 2.26[c]
V_{2Se}^{o}	1.66	0.62	D_1: 1.12–1.24; D_2: 1.70, 1.92	1.92[vi]; 2.64[b]; 2.54[c]
			WSe_2	
V_{1Se}	2.14	0.51	D_1: 1.74; Deep D_2: 2.81, 2.84; D_2: 2.61	2.04[vi]; 2.42[c]; 2.81–2.87[c]
V_{2Se}^{s}	2.09	0.65	D_1: 1.44, 1.51–1.53, 2.07; mixed D_1/D_2: 1.97–1.99; Deep D_2: 2.43	2.09[vi]; 2.42[vi]; ≥2.41[c]
V_{2Se}^{o}	2.09	0.54	D_1: 1.73, 1.80; Deep D_2: 2.77; D_2: 2.06–2.17;	2.19[a]; 2.56–2.68[c]; ≥2.71[c]

Perturbed host-like features are labeled as follows: [a] A-like; [b] A′-like; [c] higher-lying mixed/C-like. Mixed excitonic assignments are labeled as follows: [i] D_2+A'-like; [ii] Deep D_2+D_1+D_2+A'-like; [iii] D_1+A-like; [iv] Deep D_2+A-like; [v] Deep D_2+ higher-lying mixed/C-like; [vi] D_2+A-like.

References

1 Loo, A. H., Bonanni, A., Sofer, Z. & Pumera, M. Exfoliated transition metal dichalcogenides (MoS_2, $MoSe_2$, WS_2, WSe_2): An electrochemical impedance spectroscopic investigation. *Electrochemistry Communications* **50**, 39-42 (2015). https://doi.org/https://doi.org/10.1016/j.elecom.2014.10.018

2 Mayorga-Martinez, C. C., Ambrosi, A., Eng, A. Y. S., Sofer, Z. & Pumera, M. Transition metal dichalcogenides (MoS_2, $MoSe_2$, WS_2 and WSe_2) exfoliation technique has strong influence upon their capacitance. *Electrochemistry Communications* **56**, 24-28 (2015). https://doi.org/https://doi.org/10.1016/j.elecom.2015.03.017

3 Late, D. J. *et al.* Sensing Behavior of Atomically Thin-Layered MoS_2 Transistors. *ACS Nano* **7**, 4879-4891 (2013). https://doi.org/10.1021/nn400026u

4 Eftekhari, A. Molybdenum diselenide ($MoSe_2$) for energy storage, catalysis, and optoelectronics. *Applied Materials Today* **8**, 1-17 (2017). https://doi.org/https://doi.org/10.1016/j.apmt.2017.01.006

5 Chhowalla, M. *et al.* The chemistry of two-dimensional layered transition metal dichalcogenide nanosheets. *Nature chemistry* **5**, 263-275 (2013).

6 Xu, K. *et al.* Atomic-layer triangular WSe_2 sheets: synthesis and layer-dependent photoluminescence property. *Nanotechnology* **24**, 465705 (2013).

7 Zhao, Y., Zhang, Y., Yang, Z., Yan, Y. & Sun, K. Synthesis of MoS_2 and MoO_2 for their applications in H_2 generation and lithium ion batteries: a review. *Sci. Technol. Adv. Mater.* **14**, 043501 (2013). https://doi.org/10.1088/1468-6996/14/4/043501

8 Mueller, T. & Malic, E. Exciton physics and device application of two-dimensional transition metal dichalcogenide semiconductors. *npj 2D Materials and Applications* **2**, 29 (2018).

9 Wang, G. *et al.* Colloquium: Excitons in atomically thin transition metal dichalcogenides. *Reviews of Modern Physics* **90**, 021001 (2018).

10 Regan, E. C. *et al.* Emerging exciton physics in transition metal dichalcogenide heterobilayers. *Nature Reviews Materials* **7**, 778-795 (2022).

11 Hohenberg, P. & Kohn, W. Inhomogeneous Electron Gas. *Phys. Rev.* **136**, B864-B871 (1964).

12 Kohn, W. & Sham, L. J. Self-Consistent Equations Including Exchange and Correlation Effects. *Phys. Rev.* **140**, A1133-A1138 (1965).

13 Khan, M. A., Erementchouk, M., Hendrickson, J. & Leuenberger, M. N. Electronic and optical properties of vacancy defects in single-layer transition metal dichalcogenides. *Phys. Rev. B* **95**, 245435 (2017). https://doi.org/10.1103/PhysRevB.95.245435

14 Komsa, H.-P. & Krasheninnikov, A. V. Native defects in bulk and monolayer MoS_2 from first principles. *Phys. Rev. B* **91**, 125304 (2015). https://doi.org/10.1103/PhysRevB.91.125304

15 Hong, J. *et al.* Exploring atomic defects in molybdenum disulphide monolayers. *Nat. Commun.* **6**, 6293-6298 (2015).

16 Sham, L. J. & Schlüter, M. Density-Functional Theory of the Energy Gap. *Phys. Rev. Lett.* **51**, 1888-1891 (1983). https://doi.org/10.1103/PhysRevLett.51.1888

17 Qiu, D. Y., da Jornada, F. H. & Louie, S. G. Optical Spectrum of MoS_2: Many-Body Effects and Diversity of Exciton States. *Phys. Rev. Lett.* **111**, 216805 (2013). https://doi.org/10.1103/PhysRevLett.111.216805
18 Ramasubramaniam, A. Large excitonic effects in monolayers of molybdenum and tungsten dichalcogenides. *Phys. Rev. B* **86**, 115409 (2012). https://doi.org/10.1103/PhysRevB.86.115409
19 Shi, H., Pan, H., Zhang, Y.-W. & Yakobson, B. I. Quasiparticle band structures and optical properties of strained monolayer MoS_2 and WS_2. *Phys. Rev. B* **87**, 155304 (2013). https://doi.org/10.1103/PhysRevB.87.155304
20 Blase, X., Duchemin, I., Jacquemin, D. & Loos, P.-F. The Bethe–Salpeter equation formalism: From physics to chemistry. *The Journal of Physical Chemistry Letters* **11**, 7371-7382 (2020).
21 Cutkosky, R. Solutions of a Bethe-Salpeter equation. *Physical Review* **96**, 1135 (1954).
22 Leng, X., Jin, F., Wei, M. & Ma, Y. GW method and Bethe–Salpeter equation for calculating electronic excitations. *Wiley Interdisciplinary Reviews: Computational Molecular Science* **6**, 532-550 (2016).
23 Mitterreiter, E. *et al.* The role of chalcogen vacancies for atomic defect emission in MoS_2. *Nature Communications* **12**, 3822 (2021). https://doi.org/10.1038/s41467-021-24102-y
24 Jeong, T. Y. *et al.* Spectroscopic studies of atomic defects and bandgap renormalization in semiconducting monolayer transition metal dichalcogenides. *Nature Communications* **10**, 3825 (2019). https://doi.org/10.1038/s41467-019-11751-3
25 Chow, P. K. *et al.* Defect-Induced Photoluminescence in Monolayer Semiconducting Transition Metal Dichalcogenides. *ACS Nano* **9**, 1520-1527 (2015). https://doi.org/10.1021/nn5073495
26 Lee, W. *et al.* Time-resolved ARPES Determination of a Quasi-Particle Band Gap and Hot Electron Dynamics in Monolayer MoS_2. *Nano Lett.* **21**, 7363-7370 (2021). https://doi.org/10.1021/acs.nanolett.1c02674
27 Lin, Z., Yan, H., Liu, J. & An, Y. Defects engineering monolayer MoSe2 magnetic states for 2D spintronic device. *Journal of Alloys and Compounds* **774**, 160-167 (2019). https://doi.org/https://doi.org/10.1016/j.jallcom.2018.09.353
28 Burns, K. *et al.* Strain modulation using defects in two-dimensional MoS_2. *Phys. Rev. B* **102**, 085421 (2020). https://doi.org/10.1103/PhysRevB.102.085421
29 Bertoldo, F., Ali, S., Manti, S. & Thygesen, K. S. Quantum point defects in 2D materials - the QPOD database. *npj Computational Materials* **8**, 56 (2022). https://doi.org/10.1038/s41524-022-00730-w
30 Afrid, S. M. T.-S. Defect engineered magnetism induction and electronic structure modulation in monolayer MoS_2. *Heliyon* **10** (2024).
31 Blöchl, P. E. Projector augmented-wave method. *Physical review B* **50**, 17953 (1994).
32 Kresse, G. & Hafner, J. Ab initio molecular dynamics for liquid metals. *Physical review B* **47**, 558 (1993).

33 Kresse, G. & Hafner, J. Ab initio molecular-dynamics simulation of the liquid-metal–amorphous-semiconductor transition in germanium. *Physical Review B* **49**, 14251 (1994).

34 Kresse, G. & Furthmüller, J. Efficient iterative schemes for ab initio total-energy calculations using a plane-wave basis set. *Physical review B* **54**, 11169 (1996).

35 Hafner, J. Ab-initio simulations of materials using VASP: Density-functional theory and beyond. *Journal of computational chemistry* **29**, 2044-2078 (2008).

36 Perdew, J. P., Burke, K. & Ernzerhof, M. Generalized gradient approximation made simple. *Physical review letters* **77**, 3865 (1996).

37 Perdew, J. P., Burke, K. & Ernzerhof, M. Perdew, burke, and ernzerhof reply. *Physical Review Letters* **80**, 891 (1998).

38 Gant, S. E. *et al*. Optimally tuned starting point for single-shot GW calculations of solids. *Physical review materials* **6**, 053802 (2022).

39 Sander, T., Maggio, E. & Kresse, G. Beyond the Tamm-Dancoff approximation for extended systems using exact diagonalization. *Phys. Rev. B* **92**, 045209 (2015). https://doi.org/10.1103/PhysRevB.92.045209

40 Vijay, S. *et al*. Efficient periodic density functional theory calculations of charged molecules and surfaces using Coulomb kernel truncation. *Phys. Rev. B* **112**, 045409 (2025). https://doi.org/10.1103/cd6s-cdkf

41 Wu, Q., Zhang, S., Song, H.-F., Troyer, M. & Soluyanov, A. A. WannierTools: An open-source software package for novel topological materials. *Computer Physics Communications* **224**, 405-416 (2018).

42 Mostofi, A. A. *et al*. wannier90: A tool for obtaining maximally-localised Wannier functions. *Computer physics communications* **178**, 685-699 (2008).

43 Hobbs, D., Kresse, G. & Hafner, J. Fully unconstrained noncollinear magnetism within the projector augmented-wave method. *Phys. Rev. B* **62**, 11556-11570 (2000). https://doi.org/10.1103/PhysRevB.62.11556

44 McCrackin, F. L., Passaglia, E., Stromberg, R. R. & Steinberg, H. L. Measurement of the thickness and refractive index of very thin films and the optical properties of surfaces by ellipsometry. *Journal of research of the National Bureau of Standards. Section A, Physics and chemistry* **67**, 363 (1963).

45 Zhao, W. *et al*. Lattice dynamics in mono- and few-layer sheets of WS2 and WSe2. *Nanoscale* **5**, 9677-9683 (2013). https://doi.org/10.1039/C3NR03052K

46 Coehoorn, R., Haas, C. & de Groot, R. A. Electronic structure of $MoSe_2$, MoS_2, and WSe_2. II. The nature of the optical band gaps. *Phys. Rev. B* **35**, 6203-6206 (1987). https://doi.org/10.1103/PhysRevB.35.6203

47 Aspnes, D. E. Approximate solution of ellipsometric equations for optically biaxial crystals. *J. Opt. Soc. Am.* **70**, 1275-1277 (1980). https://doi.org/10.1364/JOSA.70.001275

48 Qiu, D. Y., da Jornada, F. H. & Louie, S. G. Screening and many-body effects in two-dimensional crystals: Monolayer MoS_2. *Phys. Rev. B* **93**, 235435 (2016). https://doi.org/10.1103/PhysRevB.93.235435

49 Chang Lee, V., Yue, L., Gaarde, M. B., Chan, Y.-h. & Qiu, D. Y. Many-body enhancement of high-harmonic generation in monolayer MoS_2. *Nature Communications* **15**, 6228 (2024).

50 Gao, W., Xia, W., Gao, X. & Zhang, P. Speeding up GW Calculations to Meet the Challenge of Large Scale Quasiparticle Predictions. *Sci Rep-Uk* **6**, 36849 (2016). https://doi.org/10.1038/srep36849

51 Pasquier, R., Camarasa-Gómez, M., Hehn, A.-S., Hernangómez-Pérez, D. & Wilhelm, J. Efficient GW band structure calculations using Gaussian basis functions and application to atomically thin transition-metal dichalcogenides. *Phys. Rev. B* **112**, 205130 (2025). https://doi.org/10.1103/v4zv-1pf9

52 Dimakis, N., Gupta, S., Wadud, R. & Bhatti, M. I. Dry and Hydrated Defective Molybdenum Disulfide/Graphene Bilayer Heterojunction Under Strain for Hydrogen Evolution from Water Splitting: A First-principle Study. *Comput. Mat. Sci* **205**, 111234 (2022).

53 Iberi, V. *et al.* Nanoforging single layer $MoSe_2$ through defect engineering with focused helium ion beams. *Scientific reports* **6**, 30481 (2016).

54 Chernikov, A. *et al.* Exciton Binding Energy and Nonhydrogenic Rydberg Series in Monolayer WS_2. *Phys. Rev. Lett.* **113**, 076802 (2014). https://doi.org/10.1103/PhysRevLett.113.076802

55 Gajdoš, M., Hummer, K., Kresse, G., Furthmüller, J. & Bechstedt, F. Linear optical properties in the projector-augmented wave methodology. *Phys. Rev. B* **73**, 045112 (2006). https://doi.org/10.1103/PhysRevB.73.045112

56 Timilsena, S., Gupta, S., Bhatti, M. I. & Dimakis, N. Integrated density functional theory and experimental study of optical and electronic properties for MoS_2/(Metal= Au, Pt, Ni, Cu) and MoS_2/Graphene/Metal heterointerfaces. *Surfaces and Interfaces* **67**, 106610 (2025).

57 Chang, E. K., Rohlfing, M. & Louie, S. G. Excitons and Optical Properties of a-Quartz. *Phys. Rev. Lett.* **85**, 2613-2616 (2000). https://doi.org/10.1103/PhysRevLett.85.2613

58 Onida, G., Reining, L. & Rubio, A. Electronic excitations: density-functional versus many-body Green's-function approaches. *Reviews of Modern Physics* **74**, 601-659 (2002). https://doi.org/10.1103/RevModPhys.74.601

59 Giannozzi, P. *et al.* QUANTUM ESPRESSO: a modular and open-source software project for quantum simulations of materials. **21**, 395502-395519 (2009).

60 Deslippe, J. *et al.* BerkeleyGW: A massively parallel computer package for the calculation of the quasiparticle and optical properties of materials and nanostructures. *Computer Physics Communications* **183**, 1269-1289 (2012). https://doi.org/https://doi.org/10.1016/j.cpc.2011.12.006

61 Bokdam, M. *et al.* Role of Polar Phonons in the Photo Excited State of Metal Halide Perovskites. *Sci Rep-Uk* **6**, 28618 (2016). https://doi.org/10.1038/srep28618

62 Splendiani, A. *et al.* Emerging Photoluminescence in Monolayer MoS_2. *Nano Lett.* **10**, 1271-1275 (2010).

63 Mak, K. F., Lee, C., Hone, J., Shan, J. & Heinz, T. F. Atomically Thin MoS_2: A New Direct-Gap Semiconductor. *Phys. Rev. Lett.* **105**, 136805-136804 (2010).

64 Ross, J. S. *et al.* Electrical control of neutral and charged excitons in a monolayer semiconductor. *Nature communications* **4**, 1474 (2013).
65 Arora, A., Nogajewski, K., Molas, M., Koperski, M. & Potemski, M. Exciton band structure in layered $MoSe_2$: from a monolayer to the bulk limit. *Nanoscale* **7**, 20769-20775 (2015). https://doi.org/10.1039/C5NR06782K
66 Nam, D., Lee, J.-U. & Cheong, H. Excitation energy dependent Raman spectrum of MoSe2. *Sci Rep-Uk* **5**, 17113 (2015). https://doi.org/10.1038/srep17113
67 Massicotte, M. *et al.* Dissociation of two-dimensional excitons in monolayer WSe_2. *Nature Communications* **9**, 1633 (2018). https://doi.org/10.1038/s41467-018-03864-y

Supplementary Files

This is a list of supplementary files associated with this preprint. Click to download.

- SupplementaryMaterialv2npj.docx